






## General framework for the mechanical response of metallic glasses during strain-rate-dependent uniaxial compression

Weiwei Jin <sup>1</sup>, Amit Datye <sup>1</sup>, Udo D. Schwarz <sup>1,2</sup>, Mark D. Shattuck <sup>3</sup>, and Corey S. O'Hern <sup>1,4,5,6,\*</sup>

<sup>1</sup>*Department of Mechanical Engineering and Materials Science, Yale University, New Haven, Connecticut 06520, USA*

<sup>2</sup>*Department of Chemical and Environmental Engineering, Yale University, New Haven, Connecticut 06520, USA*

<sup>3</sup>*Benjamin Levich Institute and Physics Department, The City College of New York, New York, New York 10031, USA*

<sup>4</sup>*Department of Physics, Yale University, New Haven, Connecticut 06520, USA*

<sup>5</sup>*Department of Applied Physics, Yale University, New Haven, Connecticut 06520, USA*

<sup>6</sup>*Graduate Program in Computational Biology and Bioinformatics, Yale University, New Haven, Connecticut 06520, USA*



(Received 23 May 2022; accepted 11 October 2023; published 25 October 2023)

Experimental data on compressive strength  $\sigma_{\max}$  versus strain rate  $\dot{\epsilon}_{\text{eng}}$  for metallic glasses undergoing uniaxial compression show varying strain rate sensitivity. For some metallic glasses,  $\sigma_{\max}$  decreases with increasing  $\dot{\epsilon}_{\text{eng}}$ , while for others,  $\sigma_{\max}$  increases with increasing  $\dot{\epsilon}_{\text{eng}}$ , and for certain alloys  $\sigma_{\max}$  versus  $\dot{\epsilon}_{\text{eng}}$  is nonmonotonic. To understand their strain rate sensitivity, we conduct molecular dynamics simulations of metallic glasses undergoing uniaxial compression at finite strain rates and coupled to heat baths with a range of temperatures  $T_0$  and damping parameters  $b$ . In the  $T_0 \rightarrow 0$  and  $b \rightarrow 0$  limits, we find that the compressive strength  $\sigma_{\max}$  versus temperature  $T$  obeys a “chevron-shaped” scaling relation. In the low-strain-rate regime,  $\sigma_{\max}$  decreases linearly with increasing  $T$ , whereas  $\sigma_{\max}$  grows as a power law with decreasing  $T$  in the high-strain-rate regime. For  $T_0 > 0$ ,  $\sigma_{\max}(T)$  deviates from the scaling curve at low strain rates, but  $\sigma_{\max}(T)$  rejoins the scaling curve as the strain rate increases. Enhanced dissipation reduces compression-induced heating, which causes  $\sigma_{\max}(T)$  to deviate from the  $b \rightarrow 0$  scaling behavior for intermediate strain rates, but  $\sigma_{\max}(T)$  converges to the high-strain-rate power-law scaling behavior at sufficiently high strain rates. Determining  $\sigma_{\max}(T)$  as a function of  $b$  and  $T_0$  provides a general framework for explaining the strain rate sensitivity of metallic glasses under compression.

DOI: [10.1103/PhysRevMaterials.7.105604](https://doi.org/10.1103/PhysRevMaterials.7.105604)

### I. INTRODUCTION

The combination of superior strength and hardness, large elastic limit, and high fracture toughness make bulk metallic glasses (BMGs) a promising materials class for numerous structural applications [1–4]. In contrast to conventional alloys, BMGs are amorphous (i.e., they lack long-range crystalline order), and their response to deformation is not governed by the generation and motion of topological defects. Instead, researchers have shown that shear transformation zones (STZs), where atoms undergo collective, nonaffine motion, control the mechanical response of metallic glasses. Numerous studies have probed the unique mechanical response of metallic glasses subjected to quasistatic deformations at low temperatures. However, understanding the dynamic mechanical response of metallic glasses at finite strain rates and temperatures near the glass transition temperature is important for many engineering applications.

Uniaxial compression of bulk metallic glass pillars is a common mechanical test that probes their nanoscale and microscale mechanical response. Studies have shown that the strength of BMGs under compression decreases with increasing temperature [5–7], since higher temperatures enhance the activation of shear transformation zones and formation

of shear bands [8]. However, there is no consensus about the behavior of the compressive strength as a function of strain rate for BMGs [5,9–19], where the compressive strength  $\sigma_{\max}$  is defined as the maximum engineering stress prior to steady flow. For example, as shown in Fig. 1, the compressive strength of millimeter-sized Ti- and Zr-based BMGs (such as  $\text{Ti}_{45}\text{Zr}_{16}\text{Ni}_9\text{Cu}_{10}\text{Be}_{20}$  [9],  $\text{Ti}_{40}\text{Zr}_{25}\text{Ni}_8\text{Cu}_9\text{Be}_{18}$  [10], and  $\text{Zr}_{53}\text{Cu}_{30}\text{Ni}_9\text{Al}_8$  [11]), and  $\text{Ni}_{62}\text{Nb}_{38}$  [12], increases with strain rate (i.e., positive strain rate sensitivity of  $\sigma_{\max}$ ). In contrast, the compressive strength of similar Ti- and Zr-based BMGs (e.g.,  $\text{Ti}_{32.8}\text{Zr}_{30.2}\text{Cu}_9\text{Ni}_{5.3}\text{Be}_{22.7}$  [14],  $\text{Zr}_{38}\text{Ti}_{17}\text{Cu}_{10.5}\text{Co}_{12}\text{Be}_{22.5}$  [15],  $\text{Zr}_{50.7}\text{Cu}_{28}\text{Ni}_9\text{Al}_{12.3}$  [16], and  $\text{Zr}_{52.5}\text{Cu}_{17.9}\text{Ni}_{14.6}\text{Al}_{10}\text{Ti}_5$  [17]) and  $\text{Pd}_{40}\text{Ni}_{40}\text{P}_{20}$  [13] decreases with strain rate (negative strain rate sensitivity). In addition, recent studies have shown that the compressive strength for  $\text{Zr}_{59.3}\text{Cu}_{28.8}\text{Nb}_{1.5}\text{Al}_{10.4}$  is nonmonotonic with strain rate; the strength first decreases and then increases with increasing strain rate [19]. Does the fact that different BMGs possess different strain-rate-dependent compressive strengths mean that the mechanical response of these materials depends sensitively on each particular alloy and composition? We seek to identify the dominant mechanism that controls the strain-rate-dependent compressive strength so that we can potentially describe the mechanical response of all BMGs to uniaxial compression.

In this paper, we perform molecular dynamics (MD) simulations of metallic glasses undergoing uniaxial compression

\*corey.ohern@yale.edu

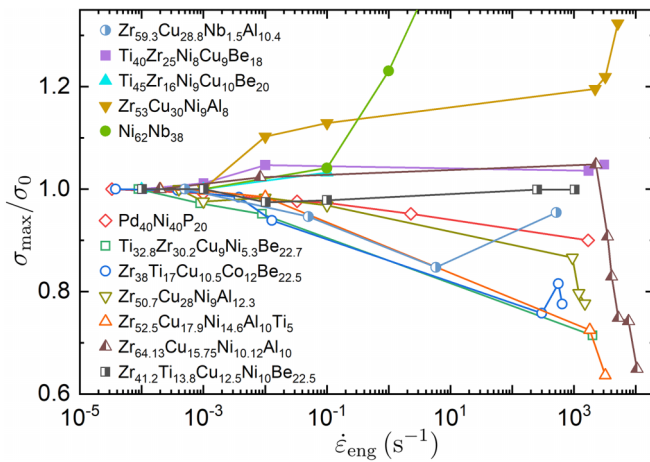


FIG. 1. Compressive strength  $\sigma_{\max}$  (normalized by the value  $\sigma_0$  at the lowest strain rate) plotted as a function of engineering strain rate  $\dot{\epsilon}_{\text{eng}}$  (in  $\text{s}^{-1}$ ) from experimental studies of 12 bulk metallic glasses undergoing uniaxial compression at room temperature [5,9–19].

using the embedded atom method (EAM) and Lennard-Jones (LJ) interatomic potentials to understand their mechanical response. Specifically, we focus on EAM simulations of  $\text{Ni}_{62}\text{Nb}_{38}$ , as well as  $\text{Zr}_{60}\text{Cu}_{29}\text{Al}_{11}$ , and LJ models of  $\text{Ni}_{62}\text{Nb}_{38}$  metallic glasses. We consider the simulation models as small subsystems embedded within a large bulk system. To account for the flow of heat from the subsystem to the bulk system (or heat bath) during compression, we incorporate a damping term proportional to the atomic velocities into the equations of motion. By varying the heat bath temperature  $T_0$  and damping coefficient  $b$ , we can effectively control the local temperature of the subsystem and the rate of heat transfer to the bulk system, respectively, during the applied compression. In addition, we focus on the preyield strain regime, where the formation and propagation of shear transformation zones are the dominant deformation mechanisms. We do not consider the formation of large-scale shear bands, which induces failure of the material.

In general, we show that the local temperature and strength of the local dissipation control the behavior of the compressive strength versus strain rate in metallic glasses. For systems coupled to a zero-temperature heat bath in the limit of low damping coefficient, the compressive strength  $\sigma_{\max}$  versus temperature  $T$  obeys a chevron-shaped scaling curve with two main branches. In the lower branch of the chevron-shaped curve,  $\sigma_{\max}$  decreases linearly with increasing  $T$ , whereas it displays a power-law increase with decreasing  $T$  in the upper branch. Higher strain rates in the lower branch contribute to more effective local heating of the system, leading to thermal softening and negative strain rate sensitivity of the compressive strength. In contrast, in the power-law upper branch, the increased potential energy from compression cannot be effectively converted into kinetic energy, which results in positive strain rate sensitivity of  $\sigma_{\max}$ . For systems coupled to a nonzero-temperature heat bath ( $T_0 > 0$ ),  $\sigma_{\max}(T)$  deviates from the scaling curve at low strain rates, but  $\sigma_{\max}(T)$  rejoins the scaling curve as the strain rate increases. For all heat bath temperatures, large damping reduces compression-induced thermal fluctuations, which causes  $\sigma_{\max}(T)$  to deviate

from, but still be bounded by, the scaling curve in the  $b \rightarrow 0$  limit.

While these computational studies have focused on two specific metallic glasses ( $\text{Ni}_{62}\text{Nb}_{38}$  and  $\text{Zr}_{60}\text{Cu}_{29}\text{Al}_{11}$ ), our results are qualitatively the same for both EAM and LJ interaction potentials and both metallic glasses. We further demonstrate that the experimental results of the compressive strength  $\sigma_{\max}$  versus the engineering strain rate  $\dot{\epsilon}_{\text{eng}}$ , as depicted in Fig. 1 for 12 different metallic glasses, can be mapped onto the same chevron-shaped scaling curves  $\sigma_{\max}(T)$  obtained from the MD simulations. Thus the chevron-shaped scaling curves in the  $\sigma_{\max}$ -versus- $T$  plane provide a general framework for understanding the strain rate sensitivity of metallic glasses.

The remainder of this paper is organized as follows. In Sec. II, we describe the cooling protocol for preparing the unstrained metallic glass samples and the uniaxial compression protocol for determining the strain-rate-dependent compressive strength of these samples. In Sec. III A, we present the results from MD simulations of  $\text{Ni}_{62}\text{Nb}_{38}$  (modeled using an EAM potential) undergoing uniaxial compression and coupled to a zero-temperature heat bath, e.g., the variation of the temperature-dependent compressive strength  $\sigma_{\max}(T)$  with damping coefficient and cooling rate used to prepare the samples. In Sec. III B, we also show results for MD simulations of  $\text{Ni}_{62}\text{Nb}_{38}$  (modeled using an EAM potential) undergoing uniaxial compression, but now the simulations are coupled to a finite-temperature heat bath  $T_0 > 0$ . We quantify how  $\sigma_{\max}(T)$  changes as  $T_0$  increases toward the glass transition temperature. In Sec. III C, we describe the methods to compare  $\sigma_{\max}(T)$  between the experimental and computational studies and different metallic glasses. We describe the deformation mechanism governing the mechanical response of metallic glasses in Sec. III D. The conclusions and promising future directions are provided in Sec. IV. We also include five Appendixes to present additional details of the MD simulations. Descriptions of the EAM and LJ atomic interactions are provided in Appendix A. In Appendix B, we show supplemental results for  $\sigma_{\max}(\dot{\epsilon}_{\text{eng}})$  and  $T(\dot{\epsilon}_{\text{eng}})$  from MD simulations of  $\text{Ni}_{62}\text{Nb}_{38}$  undergoing uniaxial compression with nonzero-temperature heat baths. The MD simulation results for uniaxial compression of  $\text{Zr}_{60}\text{Cu}_{29}\text{Al}_{11}$  modeled using an EAM interatomic potential and  $\text{Ni}_{62}\text{Nb}_{38}$  using the LJ interatomic potential are compared with  $\text{Ni}_{62}\text{Nb}_{38}$  using an EAM interatomic potential in Appendixes C and D. Finally, the fitting parameters for determining  $T(\dot{\epsilon}_{\text{eng}})$  and mapping the experimental results for  $\sigma_{\max}(\dot{\epsilon}_{\text{eng}})$  onto the simulation results for  $\sigma_{\max}(T)$  are provided in Appendix E.

## II. METHODS

In this section, we describe the computational methods to simulate uniaxial compression of metallic glasses at finite strain rates and temperatures. We conduct MD simulations of two particular BMGs,  $\text{Ni}_{62}\text{Nb}_{38}$  and  $\text{Zr}_{60}\text{Cu}_{29}\text{Al}_{11}$  [20]. The experimental measurements of the compressive strength for  $\text{Ni}_{62}\text{Nb}_{38}$  and  $\text{Zr}_{59.3}\text{Cu}_{28.8}\text{Nb}_{1.5}\text{Al}_{10.4}$  (similar to  $\text{Zr}_{60}\text{Cu}_{29}\text{Al}_{11}$ ) are shown in Fig. 1. We consider EAM interatomic potentials for  $\text{Ni}_{62}\text{Nb}_{38}$  [21] and  $\text{Zr}_{60}\text{Cu}_{29}\text{Al}_{11}$

[22] and a pairwise Lennard-Jones potential for  $\text{Ni}_{62}\text{Nb}_{38}$ . See Appendix A for the details of the interatomic potentials.

### A. Metallic glass sample preparation

Each metallic glass sample contains  $N = 6000$  atoms in a  $2 \times 2 \times 3$  cuboidal box with periodic boundary conditions in the  $x$ ,  $y$ , and  $z$  directions. The samples modeled using the EAM potentials are generated by cooling equilibrium liquid states at  $T = 2000$  K (above the glass transition temperatures  $T_g \sim 1000$  K for  $\text{Ni}_{62}\text{Nb}_{38}$  and  $T_g \sim 850$  K for  $\text{Zr}_{60}\text{Cu}_{29}\text{Al}_{11}$ ) to a target temperature  $0 < T_0 \leq 120$  K using a range of cooling rates from  $R = 10^{10}$  K/s to  $R = 10^{13}$  K/s. The temperature of the system is calculated using  $T = 2\mathcal{K}/(3Nk_B)$ , where  $\mathcal{K}$  is the total kinetic energy and  $k_B$  is the Boltzmann constant. After quenching the system to  $T_0 < T_g$ , we change the periodic boundary conditions in the  $x$  and  $y$  directions to open boundary conditions, such that the pressure in the transverse direction is effectively zero, mimicking the experimental compression of micropillars. The periodic boundary conditions in the  $z$  direction (i.e., the direction in which the compression is later applied) are maintained to minimize the effects of a physical boundary in small systems. The system is relaxed using the Nosé-Hoover thermostat and barostat (using the velocities and system size in the  $z$  direction as the degrees of freedom) to achieve zero pressure at temperature  $T_0$ .

The  $\text{Ni}_{62}\text{Nb}_{38}$  metallic glass samples modeled with the LJ interatomic potential are generated using a similar geometry and protocol to those used for the metallic glass samples modeled using the EAM potentials. Using periodic boundary conditions in the  $x$ ,  $y$ , and  $z$  directions, we cool equilibrium liquid states at  $T = 2 \times 10^4$  K to low temperature,  $T_0 = 20$  K, over a range of cooling rates from  $R = 10^{12}$  K/s to  $R = 10^{14}$  K/s. We then open the boundaries in the  $x$  and  $y$  directions and bring the system to zero pressure at temperature  $T_0$  using the Nosé-Hoover thermostat and barostat. For the LJ interaction potential, we use  $\sigma_{\text{NbNb}} = 3 \times 10^{-10}$  m,  $\sigma_{\text{NbNb}}\sqrt{m_{\text{Nb}}/\epsilon_{\text{NbNb}}} = 5.4 \times 10^{-13}$  s,  $\epsilon_{\text{NbNb}}/\sigma_{\text{NbNb}}^2 = 1.7$  GPa, and  $\epsilon_{\text{NbNb}}/k_B = 3400$  K as the length, time, stress, and temperature scales, respectively.

### B. Uniaxial compression protocol

We subject the metallic glass samples to uniaxial compression at nonzero strain rates  $\dot{\epsilon}_{\text{eng}}$  in the  $z$  direction. The engineering strain and stress are defined as

$$\epsilon_{\text{eng}} = (L_{z0} - L_z)/L_{z0}, \quad (1)$$

$$\sigma_{\text{eng}} = F_z/A_0, \quad (2)$$

where  $L_{z0}$  is the initial sample length in the  $z$  direction,  $A_0$  is the initial cross-sectional area in the  $x$ - $y$  plane, and  $F_z$  is the total force in the  $z$  direction that opposes the compressive strain. The strain is applied affinely to the system, such that after each compressive strain increment,  $\Delta\epsilon_{\text{eng}} = \dot{\epsilon}_{\text{eng}}\Delta t$ , the new  $z$  position of each atom  $i$  is  $z'_i = z_i(1 - \Delta\epsilon_{\text{eng}})$ , where  $\Delta t$  is the time step. The compressive strength  $\sigma_{\text{max}}$  is defined as the maximum in  $\sigma_{\text{eng}}(\epsilon_{\text{eng}})$  prior to steady flow.

We conduct MD simulations on metallic glass samples containing  $N = 6000$  atoms, which are much smaller than the micrometer-sized experimental samples in Fig. 1. We consider the simulation as a small subsystem coupled to the rest of the bulk sample, which represents a heat bath (at temperature  $T_0$ ) that can inject and remove heat from the subsystem. It is straightforward to show that after integrating over the degrees of freedom for the heat bath in the coupled system, the equations of motion for the atomic degrees of freedom in the subsystem include a noise term and a damping term proportional to the atomic velocities. The damping term represents the flow of heat from the subsystem to the heat bath, and the noise term represents heat flow from the heat bath to the subsystem.

We implement a Langevin thermostat [23] to model the heat bath at temperature  $T_0$ . In this case, the force acting on atom  $i$  with mass  $m_i$  is

$$\mathbf{F}_i = \mathbf{F}_i^c + \mathbf{F}_i^d + \mathbf{F}_i^n = m_i\mathbf{a}_i, \quad (3)$$

where  $\mathbf{a}_i$  is the acceleration of atom  $i$ ,  $\mathbf{F}_i^c = -\partial U/\partial \mathbf{r}_i$  is the conservative force arising from the total potential energy  $U$ ,  $\mathbf{F}_i^d = -b\mathbf{v}_i$  is the damping force proportional to the velocity  $\mathbf{v}_i$  of atom  $i$ , and  $\mathbf{F}_i^n$  is the noise term that is directed in a random direction and has a magnitude proportional to  $\sqrt{k_B T_0 b/\Delta t}$ . For a zero-temperature heat bath,  $\mathbf{F}_i^n = 0$ . We vary the damping coefficient  $b$  to tune the time scale of the heat flow from the subsystem to the heat bath. The integration scheme for Eq. (3) is a modified velocity-Verlet algorithm with time step  $\Delta t = 0.002$  ps [24].

In addition to computational studies of uniaxial compression carried out at finite strain rates, we also subjected the metallic glass samples to athermal, quasistatic uniaxial compression [25]. For this method, we applied successive compressive strain increments  $\Delta\epsilon_{\text{eng}} = 2 \times 10^{-5}$  with each increment followed by potential energy minimization using the conjugate gradient algorithm.

## III. RESULTS

In this section, we describe the results for the MD simulations of  $\text{Ni}_{62}\text{Nb}_{38}$  metallic glass samples undergoing uniaxial compression. In Sec. III A, we show the results for the compressive strength of metallic glass samples undergoing uniaxial compression and coupled to a zero-temperature heat bath. In particular, we illustrate the chevron-shaped scaling behavior of  $\sigma_{\text{max}}(T)$  in the low-damping-coefficient limit and how it is modified with increasing  $b$ . In Sec. III B, we determine how  $\sigma_{\text{max}}(T)$  changes with increases in the heat bath temperature  $T_0$ . We describe the methods to map the MD simulation results for  $\sigma_{\text{max}}(T)$  at nonzero heat bath temperatures onto those at  $T_0 = 0$  and for mapping the experimental data for  $\sigma_{\text{max}}(\dot{\epsilon}_{\text{eng}})$  onto  $\sigma_{\text{max}}(T)$  from the MD simulations in Sec. III C. Finally, we introduce a general framework for understanding the strain rate sensitivity of  $\sigma_{\text{max}}$  in metallic glasses in Sec. III D. Additional simulation results for  $\text{Ni}_{62}\text{Nb}_{38}$  and  $\text{Zr}_{60}\text{Cu}_{29}\text{Al}_{11}$  undergoing uniaxial compression at zero and nonzero temperature heat baths are provided in Appendixes B, C, and D.

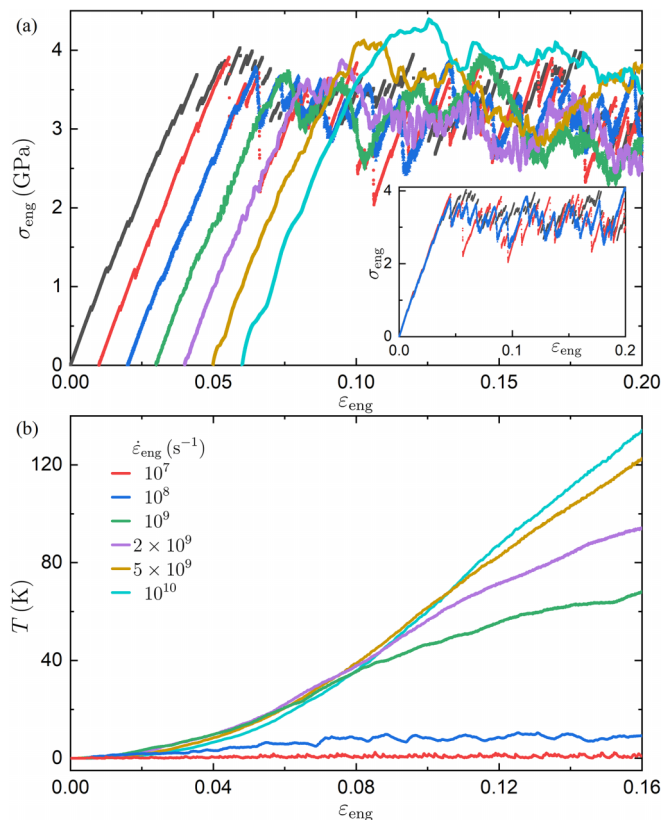


FIG. 2. (a) Engineering stress  $\sigma_{\text{eng}}$  vs strain  $\varepsilon_{\text{eng}}$  from EAM simulations of uniaxial compression of a  $\text{Ni}_{62}\text{Nb}_{38}$  sample obtained using cooling rate  $R = 10^{12}$  K/s. The black curve corresponds to athermal, quasistatic compression, and the horizontally shifted curves, from left to right, correspond to compression coupled to a zero-temperature heat bath with damping coefficient  $b = 10^{-4}$  eV ps Å<sup>-2</sup> at strain rates  $\dot{\varepsilon}_{\text{eng}} = 10^7$  (red),  $10^8$  (blue),  $10^9$  (green),  $2 \times 10^9$  (magenta),  $5 \times 10^9$  (orange), and  $10^{10}$  (cyan) s<sup>-1</sup>, respectively. The inset shows the same data for  $\sigma_{\text{eng}}$  vs  $\varepsilon_{\text{eng}}$  in the main panel for athermal, quasistatic compression and  $\dot{\varepsilon}_{\text{eng}} = 10^7$  and  $10^8$  s<sup>-1</sup> without horizontally shifting the data. (b) Average temperature  $T$  vs strain  $\varepsilon_{\text{eng}}$  from EAM simulations of 20  $\text{Ni}_{62}\text{Nb}_{38}$  samples prepared using  $R = 10^{12}$  K/s for each strain rate. The damping coefficient and strain rate color codes are the same as those in (a).

### A. Zero-temperature heat bath

We first present the results of the MD simulations of uniaxial compression (coupled to a zero-temperature heat bath) of  $\text{Ni}_{62}\text{Nb}_{38}$  metallic glass samples modeled using an EAM potential. In Fig. 2(a), we show the stress-versus-strain relation for samples compressed at several strain rates and fixed damping coefficient,  $b = 10^{-4}$  eV ps Å<sup>-2</sup>. At low strain rates, the stress-strain curves possess quasilinear elastic segments, punctuated by discontinuous drops in the stress. In particular, the stress-strain curves for  $\dot{\varepsilon}_{\text{eng}} \lesssim 10^8$  s<sup>-1</sup> agree with those obtained using athermal, quasistatic compression as shown in the inset in Fig. 2(a). Serrations in the stress-strain relations have also been found in experimental studies of uniaxial compression and nanoindentation of BMGs at low strain rates [19,26]. The stress-strain curves become more continuous, and the maximum stress is nonmonotonic with increasing strain rate. For  $\dot{\varepsilon}_{\text{eng}} = 10^8$  s<sup>-1</sup>, the maximum stress value de-

creases below that achieved in the low-strain-rate limit. As the strain rate increases further, i.e., for  $\dot{\varepsilon}_{\text{eng}} \gtrsim 5 \times 10^9$  s<sup>-1</sup>, the maximum stress is larger than that in the low-strain-rate limit. In Fig. 2(b), we show the variation of the internal temperature  $T$  as a function of strain  $\varepsilon_{\text{eng}}$  at fixed damping coefficient and different strain rates. For a given damping coefficient and strain rate, the temperature of the system will increase from its initial value (in this case,  $T_0 = 0$ ) and then reach a steady-state value  $T_f$  after a given total compressive strain  $\varepsilon_f$ . The steady-state  $T_f$  is determined by balancing the compression-induced heating (from the applied strain rate) and heat removal (to the heat bath) arising from damping. Both  $T_f$  and  $\varepsilon_f$  increase with increasing strain rate but decrease with increasing damping coefficient. For  $\dot{\varepsilon}_{\text{eng}} \gtrsim 2 \times 10^9$  s<sup>-1</sup>, we do not show the strain regime where  $T \rightarrow T_f$  in Fig. 2(b).

The stress-strain relations for metallic glasses depend on the damping coefficient and strain rate, as well as the cooling rate used to prepare the sample. The results for the compressive strength as a function of the strain rate for EAM simulations of  $\text{Ni}_{62}\text{Nb}_{38}$  prepared using different cooling rates and compressed in contact with a zero-temperature heat bath at different damping coefficients are shown in Fig. 3(a). We find that the compressive strength  $\sigma_{\text{max}}$  has a self-similar form for different cooling rates, where the compressive strength increases with decreasing cooling rate. This behavior can be attributed to the dependence of the mechanical properties of glasses on the depth of potential energy minima that they sample. Lower cooling rates allow the system to explore and sample deeper energy minima, leading to enhanced mechanical properties, including higher compressive strength. We therefore plot the cooling-rate-scaled and averaged compressive strength

$$\sigma_{\text{max}}^* = \langle \sigma_{\text{max}}(R/R_c)^\gamma \rangle_R, \quad (4)$$

where  $\gamma \approx 0.038$  and  $R_c = 1$  K/s is a reference cooling rate, versus strain rate in Fig. 3(b) to remove the cooling rate dependence.  $\langle \cdot \rangle_R$  indicates the average of  $\sigma_{\text{max}}(R/R_c)^\gamma$  over the four cooling rates,  $R = 10^{10}, 10^{11}, 10^{12}$ , and  $10^{13}$  K/s. (Changing  $R_c$  will only modify  $\sigma_{\text{max}}^*$  by a constant multiplicative factor.) The exponent  $\gamma$  is obtained by finding the best collapse for  $\sigma_{\text{max}}^*$  over the full range of cooling rates. We find several important features for  $\sigma_{\text{max}}^*(\dot{\varepsilon}_{\text{eng}})$ . First, in the low-strain-rate limit (for the nonzero damping coefficients considered),  $\sigma_{\text{max}}^*$  approaches the value obtained for athermal quasistatic compression. Second, the scaled compressive strength increases monotonically with strain rate when the damping coefficient  $b = 0$ , whereas  $\sigma_{\text{max}}^*$  is nonmonotonic in  $\dot{\varepsilon}_{\text{eng}}$  when  $b > 0$  [19], i.e., the scaled compressive strength first decreases with increasing strain rate and then increases rapidly for  $\dot{\varepsilon}_{\text{eng}} \gtrsim 10^9$  s<sup>-1</sup>. The magnitude of the nonmonotonic behavior [i.e., the difference between the value of  $\sigma_{\text{max}}^*$  at  $\dot{\varepsilon}_{\text{eng}} \rightarrow 0$  and the minimal value of  $\sigma_{\text{max}}^*(\dot{\varepsilon}_{\text{eng}})$ ] across the strain rate range increases with decreasing  $b$ .

To understand the nonmonotonic behavior of  $\sigma_{\text{max}}^*$  versus  $\dot{\varepsilon}_{\text{eng}}$ , we characterize the local temperature of the system during compression. We show the temperature averaged over strains in the range  $0 < \varepsilon_{\text{eng}} < \varepsilon_b$  versus the strain rate for samples prepared using several cooling rates,  $R = 10^{10}, 10^{11}, 10^{12}$ , and  $10^{13}$  K/s in Fig. 4(a). (For  $\varepsilon_b \sim 0.084$ ,  $\sigma_{\text{max}}^*$  occurs in this strain interval for all systems considered.) As we found

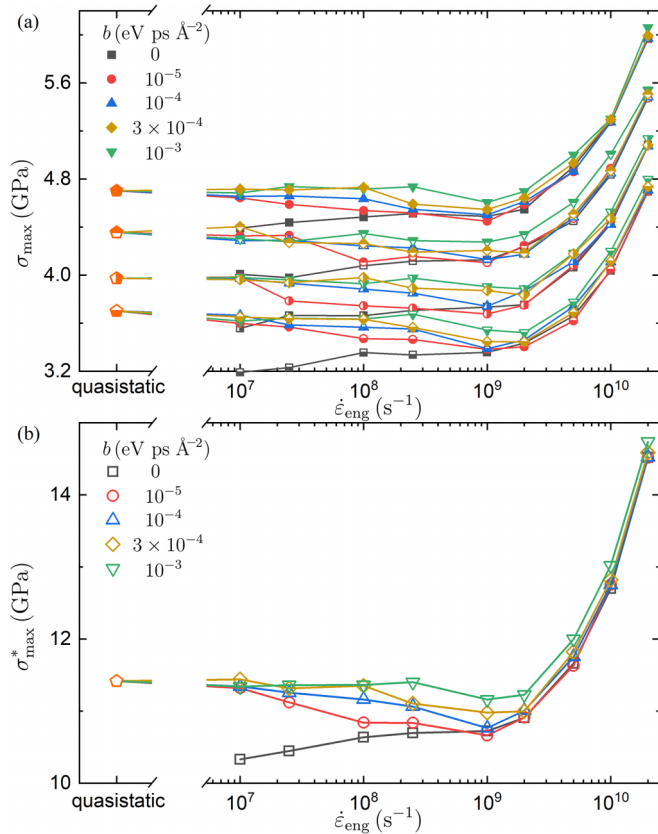


FIG. 3. (a) Compressive strength  $\sigma_{\max}$  plotted as a function of strain rate  $\dot{\epsilon}_{\text{eng}}$  for  $\text{Ni}_{62}\text{Nb}_{38}$  samples (modeled using an EAM potential) undergoing uniaxial compression with a zero-temperature heat bath. Samples were generated using a range of cooling rates,  $R = 10^{10}$  (fully filled symbols),  $10^{11}$  (top-filled),  $10^{12}$  (right-filled), and  $10^{13}$  (bottom-filled) K/s, and five damping coefficients  $b$ . (b) Compressive strength  $\sigma_{\max}^*$  (scaled by the cooling rate used to prepare the samples) in Eq. (4) plotted vs strain rate  $\dot{\epsilon}_{\text{eng}}$  for  $\text{Ni}_{62}\text{Nb}_{38}$  (averaged over 80 samples) at several damping coefficients  $b$ . The data for athermal quasistatic compression are shown as pentagons.

for the compressive strength, the temperature versus strain rate has a self-similar form for different cooling rates used to prepare the samples. Thus we can effectively remove the cooling-rate dependence by scaling  $T - T_0$ . In Fig. 4(b), we plot the cooling-rate-scaled and averaged temperature,

$$T^* = \langle (T - T_0)(R/R_c)^{-\lambda} \rangle_R, \quad (5)$$

where  $\lambda \approx 0.057$  and  $R_c = 1$  K/s is a reference cooling rate. Changing  $R_c$  will only change  $T^*$  by a constant multiplicative factor. The strain rate dependence of the cooling-rate-scaled and averaged temperature can be captured by the expression

$$T^*(\dot{\epsilon}) = \frac{c(\dot{\epsilon}/k)^\alpha}{1 + (\dot{\epsilon}/k)^\beta}, \quad (6)$$

where the coefficients  $k$  and  $c$  have units of s $^{-1}$  and K, respectively, and the power-law exponents  $\alpha$  and  $\beta$  depend on  $b$ . The values of  $k$ ,  $c$ ,  $\alpha$ , and  $\beta$  are provided in Table I of Appendix E. For systems with  $b = 0$ , in which compression-induced energy increases are not dissipated, the exponent  $\alpha$  is equal to zero and  $\beta > 0$ , indicating that the cooling-rate-

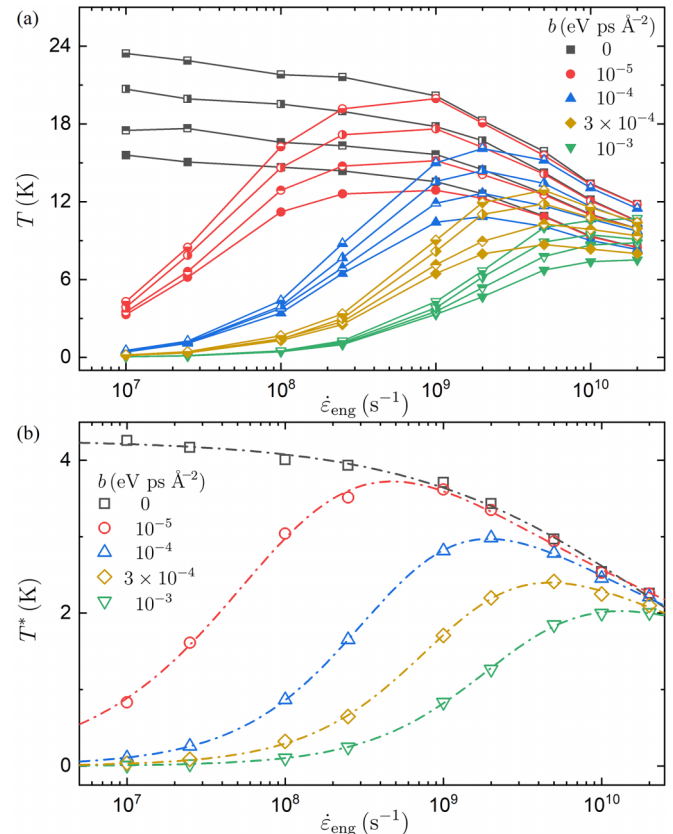


FIG. 4. (a) Average temperature  $T$  (over the strain interval  $0 < \epsilon_{\text{eng}} < \epsilon_b$ ) plotted vs  $\dot{\epsilon}_{\text{eng}}$  for the systems in Fig. 3(a). The symbol style is the same as in Fig. 3(a). Similar  $T(\dot{\epsilon}_{\text{eng}})$  curves are obtained for samples prepared over a wide range of cooling rates. (b) Cooling-rate-scaled and averaged temperature  $T^*$  in Eq. (5) vs  $\dot{\epsilon}_{\text{eng}}$ . Best fits of  $T^*(\dot{\epsilon}_{\text{eng}})$  to Eq. (6) for different  $b$  values are shown as dash-dotted lines.

scaled and averaged temperature  $T^*$  decreases monotonically with increasing strain rate. This monotonic decrease occurs because the averaging strain interval is fixed, and as the strain rate increases, the system has less time to heat up during compression. For systems with  $b > 0$ , in which heat flows from the subsystem to the surrounding bulk system, the exponents  $\alpha$  and  $\beta$  satisfy  $\beta > \alpha$  and  $\alpha > 0$ . This form for  $T^*$  suggests that the temperature-versus-strain-rate curves exhibit a maximum, indicating that beyond a dimensionless strain rate  $m\dot{\epsilon}_{\text{eng}}/b \gg 1$ , where  $m$  is the average mass per atom, the strain rate is so fast that sufficient time has not elapsed to allow the additional potential energy resulting from compression to be efficiently converted into kinetic energy. At low strain rates, the damping can effectively remove heat from the system during compression, and thus the temperature at low strain rates decreases with increasing damping coefficient. As the strain rate is increased, damping is less effective at removing heat, and the temperature increases with strain rate. We find that the position  $\dot{\epsilon}_p$  of the peak in  $T^*(\dot{\epsilon}_{\text{eng}})$  scales linearly with  $b$ , while the peak value of  $T^*$  scales as  $\dot{\epsilon}_p^{-\mu}$ , with  $\mu \sim 0.2$ .

The results in Figs. 3 and 4 suggest that the nonmonotonic behavior of  $\sigma_{\max}$  versus  $\dot{\epsilon}_{\text{eng}}$  is caused by the nonmonotonic dependence of temperature on strain rate. Therefore we plot the cooling-rate-scaled and averaged compressive strength

TABLE I. Parameters for fits of  $T^*(\dot{\epsilon}_{\text{eng}})$  from MD simulations of uniaxial compression of  $\text{Ni}_{62}\text{Nb}_{38}$  [Figs. 4(b) and 12] and  $\text{Zr}_{60}\text{Cu}_{29}\text{Al}_{11}$  [Fig. 14(b)] to Eq. (6) for varying heat bath temperatures  $T_0$  and damping coefficients  $b$  (eV ps  $\text{\AA}^{-2}$ ).

Figure	$b$	$k$	$c$	$\alpha$	$\beta$
	0	$2.26 \times 10^{10}$	4.27	0	0.564
Fig. 4(b)	$10^{-5}$	$1.09 \times 10^8$	6.12	0.767	0.956
$T_0 = 0$ K	$10^{-4}$	$5.28 \times 10^8$	4.77	0.947	1.16
$\text{Ni}_{62}\text{Nb}_{38}$	$3 \times 10^{-4}$	$1.27 \times 10^9$	3.80	0.988	1.19
	$10^{-3}$	$2.90 \times 10^9$	3.07	1.00	1.17
Fig. 12(a)	0	$2.35 \times 10^{10}$	4.31	0	0.518
$T_0 = 2$ K	$6 \times 10^{-5}$	$3.02 \times 10^8$	5.02	0.922	1.11
$\text{Ni}_{62}\text{Nb}_{38}$	$2 \times 10^{-4}$	$1.29 \times 10^9$	4.61	0.851	1.12
Fig. 12(b)	0	$2.04 \times 10^{10}$	4.36	0	0.494
$T_0 = 10$ K	$7 \times 10^{-6}$	$6.44 \times 10^7$	5.95	0.750	0.916
$\text{Ni}_{62}\text{Nb}_{38}$	$6 \times 10^{-5}$	$2.86 \times 10^8$	4.87	0.944	1.13
Fig. 12(c)	0	$8.45 \times 10^9$	4.61	0	0.378
$T_0 = 40$ K	$6 \times 10^{-5}$	$2.71 \times 10^8$	4.52	0.977	1.17
$\text{Ni}_{62}\text{Nb}_{38}$	$5 \times 10^{-4}$	$1.06 \times 10^9$	2.90	1.10	1.24
Fig. 12(d)	0	$4.15 \times 10^8$	5.88	0	0.292
$T_0 = 120$ K	$7 \times 10^{-6}$	$3.98 \times 10^7$	4.88	0.886	1.08
$\text{Ni}_{62}\text{Nb}_{38}$	$6 \times 10^{-5}$	$2.33 \times 10^8$	3.81	0.979	1.21
	0	$1.54 \times 10^{10}$	22.2	0	0.516
Fig. 14(b)	$10^{-5}$	$1.06 \times 10^8$	30.7	0.828	1.03
$T_0 = 0$ K	$10^{-4}$	$4.61 \times 10^8$	22.8	1.02	1.23
$\text{Zr}_{60}\text{Cu}_{29}\text{Al}_{11}$	$10^{-3}$	$1.95 \times 10^9$	12.5	1.17	1.27

$\sigma_{\text{max}}^*$  versus the scaled and averaged temperature  $T^*$  for EAM simulations of  $\text{Ni}_{62}\text{Nb}_{38}$  undergoing uniaxial compression with coupling to a zero-temperature heat bath in Fig. 5. In the limit of low damping coefficient ( $b \rightarrow 0$ ),  $\sigma_{\text{max}}^*$  versus  $T^*$  follows a chevron-shaped scaling curve, which consists of two main branches. In the lower branch, which corre-

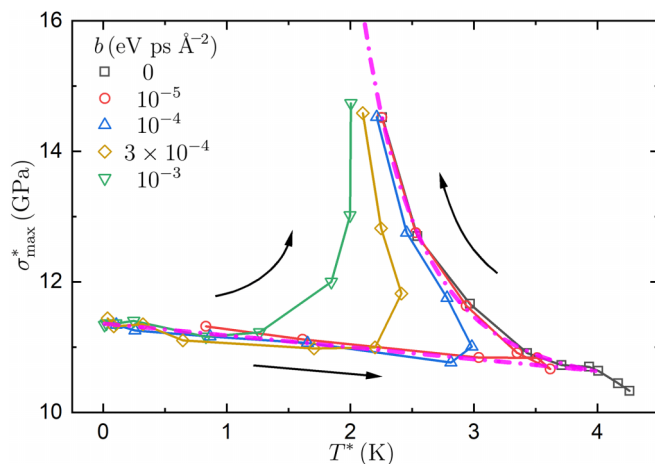


FIG. 5. Cooling-rate-scaled and averaged compressive strength  $\sigma_{\text{max}}^*$  plotted as a function of the cooling-rate-scaled and averaged temperature  $T^*$  for  $\text{Ni}_{62}\text{Nb}_{38}$  samples [using data from Figs. 3(b) and 4(b)] undergoing uniaxial compression with coupling to a zero-temperature heat bath at several damping coefficients  $b$ . The arrows indicate the directions of the increasing strain rate. The magenta dash-dotted lines give the chevron-shaped scaling behavior in the  $b \rightarrow 0$  limit.

sponds to the low-strain-rate regime,  $\sigma_{\text{max}}^*$  decreases linearly with increasing  $T^*$ , following  $\sigma_{\text{max}}^* = \sigma_1 - \kappa T^*$ , where  $\sigma_1$  is the scaled compressive strength in the  $T^* \rightarrow 0$  limit and  $\kappa \approx 0.18$  GPa/K. When the cooling-rate-scaled and averaged temperature reaches  $T^* \approx 4$  K, further increases in strain rate cause the scaled temperature to *decrease*, and  $\sigma_{\text{max}}^*$  increases as a power law with decreasing temperature,  $\sigma_{\text{max}}^* \sim (T^*)^{-\nu}$ , with  $\nu \approx 4.6$ . For systems with nonzero damping coefficients,  $\sigma_{\text{max}}^*(T^*)$  deviates from the chevron-shaped scaling behavior at a  $T^*$  that depends on  $b$ . In particular, in the limit of high damping coefficient, initial increases in strain rate cause only relatively small temperature increases, and the compressive strength does not decrease significantly. With further increases in strain rate, the temperature starts to decrease, and the compressive strength increases rapidly, eventually approaching the  $\sigma_{\text{max}}^* \sim (T^*)^{-\nu}$  power-law scaling relation. These results emphasize the effects of strain rate and damping coefficient in determining the local temperature, which in turn controls the compressive strength in metallic glasses undergoing uniaxial compression with coupling to a zero-temperature heat bath.

## B. Finite-temperature heat bath

In this section, we present results for EAM simulations of  $\text{Ni}_{62}\text{Nb}_{38}$  metallic glasses subjected to uniaxial compression, but coupled to a heat bath at *nonzero* temperatures (i.e.,  $T_0 = 2, 10, 40,$  and  $120$  K). As shown in Sec. III A, the compressive strength of metallic glasses prepared using different cooling rates is self-similar, and thus we show results for the cooling-rate-scaled compressive strength and temperature. (However, we only include the results for  $\sigma_{\text{max}}^*$  and  $T^*$  at  $T_0 > 0$  for samples prepared using a single cooling rate of  $10^{10}$  K/s.) As shown in Fig. 6(a),  $\sigma_{\text{max}}^*$  versus  $T^*$  for systems compressed using a low-temperature heat bath (i.e.,  $T_0 = 2$  and  $10$  K) is similar to that for systems compressed using a zero-temperature heat bath. In particular,  $\sigma_{\text{max}}^*$  decreases linearly with increasing  $T^*$  in the lower branch of the chevron-shaped curve and grows as a power law with decreasing  $T^*$  in the upper branch of the chevron-shaped curve. However, for heat baths with  $T_0 \gtrsim 40$  K, the  $\sigma_{\text{max}}^*$ -versus- $T^*$  curves shift to smaller values of  $\sigma_{\text{max}}^*$  and  $T^*$ , and  $\sigma_{\text{max}}^*$  *increases* (rather than decreases) with increasing  $T^*$  at the beginning of the lower branch of the chevron-shaped curve.

For systems coupled to a heat bath at higher temperatures, as shown in Fig. 6(b), the nonmonotonic behavior of  $\sigma_{\text{max}}^*$  versus  $\dot{\epsilon}_{\text{eng}}$  can be recovered at sufficiently small damping coefficients (and certain strain rates), where  $\sigma_{\text{max}}^*$  first increases with increasing  $T^*$  at low strain rates, then decreases with increasing  $T^*$  at intermediate strain rates, and finally increases as a power law with decreasing  $T^*$  at the highest strain rates. We find similar results for  $\sigma_{\text{max}}^*$  versus  $T^*$  for heat bath temperatures  $T_0 = 2, 10,$  and  $40$  K. (See Appendix B.) The fact that we obtain the nonmonotonic behavior for  $\sigma_{\text{max}}^*$  versus  $\dot{\epsilon}_{\text{eng}}$  over such a wide range of heat bath temperatures emphasizes the generality of these results.

## C. Comparing compressive strength versus temperature in simulations and experiments

As shown in Sec. III B,  $\text{Ni}_{62}\text{Nb}_{38}$  metallic glass samples (modeled with EAM atomic interactions) undergoing uniaxial

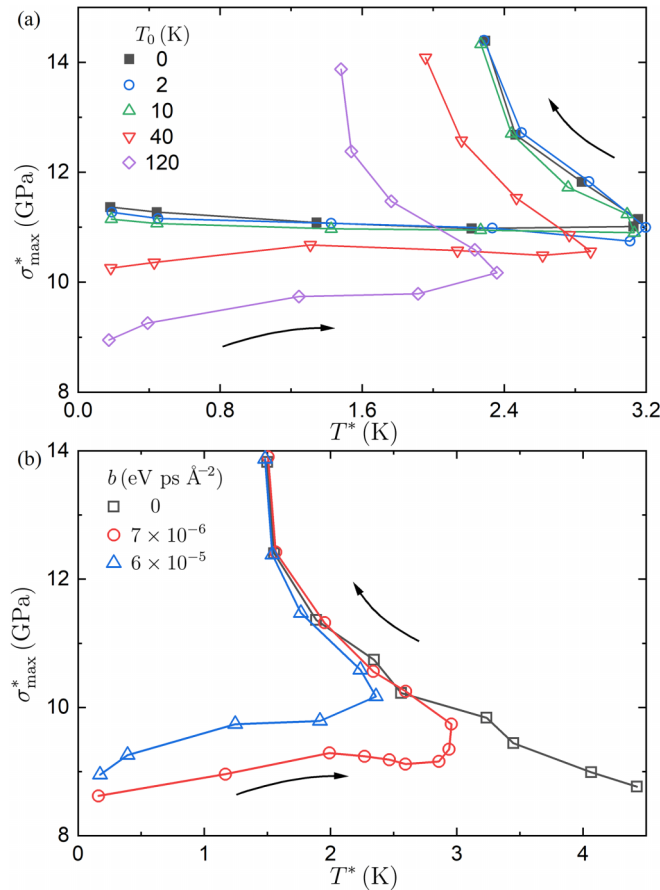


FIG. 6. (a) Cooling-rate-scaled compressive strength  $\sigma_{\max}^*$  plotted vs the cooling-rate-scaled temperature  $T^*$  from MD simulations of uniaxial compression of  $\text{Ni}_{62}\text{Nb}_{38}$  (modeled using EAM atomic interactions) with coupling to a heat bath at  $T_0 = 0, 2, 10, 40,$  and  $120$  K. The damping coefficient  $b$  is  $6 \times 10^{-5}$  eV ps  $\text{\AA}^{-2}$  for all simulations. (b)  $\sigma_{\max}^*$  plotted vs  $T^*$  for the same simulations in (a) with heat bath  $T_0 = 120$  K and several damping coefficients  $b$ . The solid arrows in (a) and (b) indicate the directions of increasing strain rate.

compression and coupled to a finite-temperature heat bath obey  $\sigma_{\max}^*$ -versus- $T^*$  relations similar to those of samples coupled to a zero-temperature heat bath. Thus we seek to map the results for  $\sigma_{\max}^*$  versus  $T^*$  for systems with a nonzero-temperature heat bath onto  $\sigma_{\max}^\dagger$  versus  $T^\dagger$  for systems with a zero-temperature heat bath by applying linear transformations to  $\sigma_{\max}^*$  and  $T^*$  for the systems at  $T_0 > 0$ . In particular, we set

$$\begin{aligned} \sigma_{\max}^\dagger &= k_{\sigma,s} \sigma_{\max}^* + c_{\sigma,s}, \\ T^\dagger &= k_{T,s} T^* + c_{T,s}, \end{aligned} \quad (7)$$

where the coefficients  $k_{\sigma,s}$ ,  $c_{\sigma,s}$ ,  $k_{T,s}$ , and  $c_{T,s}$  (listed in Table II of Appendix E) are selected so that the region with negative strain rate sensitivity and the upper power-law branch of  $\sigma_{\max}^\dagger$  versus  $T^\dagger$  for systems at  $T_0 > 0$  with low damping coefficients match the lower and upper branches of the chevron-shaped scaling curves of  $\sigma_{\max}^*$  versus  $T^*$  at  $T_0 = 0$ . The  $T_0$ -dependent coefficients obtained from this procedure at low  $b$  are used to scale  $\sigma_{\max}^*$  and  $T^*$  at the same  $T_0$  and higher damping coefficients. (This set of linear transformations is referred to as method I.) The scaled simulation data for zero and nonzero

TABLE II. Parameters for the linear transformation in Eq. (7) that map the results for the EAM simulations of  $\text{Ni}_{62}\text{Nb}_{38}$  undergoing uniaxial compression and coupled to a finite-temperature heat bath to those coupled to a zero-temperature heat bath, as shown in Fig. 7.

Heat bath	$k_{\sigma,s}$	$c_{\sigma,s}$	$k_{T,s}$	$c_{T,s}$
$T_0 = 2$ K	1.05	-0.551	0.902	0.198
$T_0 = 10$ K	1.06	-0.485	0.782	0.430
$T_0 = 40$ K	0.970	0.671	0.979	0.242
$T_0 = 120$ K	0.784	3.68	0.538	1.35

heat bath temperatures are shown in Fig. 7. At  $T_0 = 0$ , the chevron-shaped scaling curve  $\sigma_{\max}^\dagger(T^\dagger)$  is characterized by a lower branch that decreases linearly with the scaled temperature and an upper branch that grows as a power law with decreasing temperature. In contrast, for  $T_0 > 0$ ,  $\sigma_{\max}^\dagger$  initially increases with  $T^\dagger$  at the lowest strain rates, and then at higher strain rates the compressive strength versus temperature obeys the same scaling behavior as that observed for  $T_0 = 0$  and varying damping coefficients.

As discussed in Appendixes C and D, we also performed MD simulations of uniaxial compression of  $\text{Zr}_{60}\text{Cu}_{29}\text{Al}_{11}$  (modeled with an EAM atomic interaction) and  $\text{Ni}_{62}\text{Nb}_{38}$  (modeled with Lennard-Jones interactions) coupled to a zero-temperature heat bath and find qualitatively the same behavior for the compressive strength versus temperature as found for the  $\text{Ni}_{62}\text{Nb}_{38}$  metallic glass samples modeled using EAM atomic interactions. Again,  $\sigma_{\max}^\dagger$  decreases linearly with increasing  $T^\dagger$  in the low-strain-rate branch and grows as a

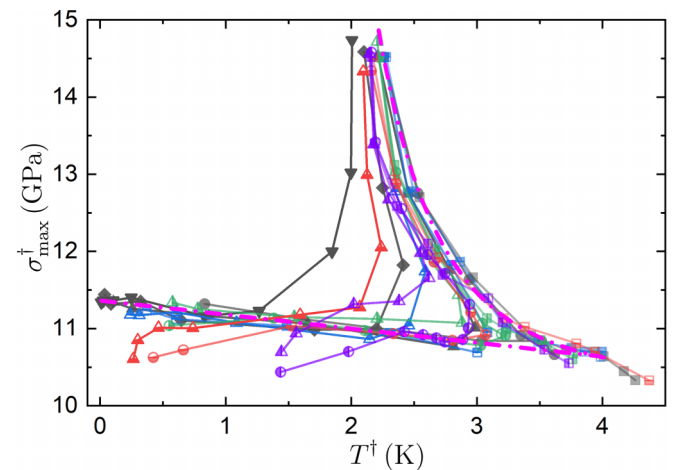


FIG. 7. Scaled compressive strength  $\sigma_{\max}^\dagger$  plotted vs the scaled temperature  $T^\dagger$  [Eq. (7)] for all MD simulations of  $\text{Ni}_{62}\text{Nb}_{38}$  metallic glasses (modeled using EAM interactions) undergoing uniaxial compression and coupled to a heat bath with  $T_0 = 0, 2, 10, 40,$  and  $120$  K. Black fully filled, blue top-filled, green right-filled, red bottom-filled, and purple left-filled symbols correspond to the heat bath with  $T_0 = 0, 2, 10, 40,$  and  $120$  K, respectively. Squares, circles, upward triangles, diamonds, and downward triangles correspond to increasing damping coefficients from 0 to  $10^{-3}$  eV ps  $\text{\AA}^{-2}$ . The magenta dash-dotted lines indicate the chevron-shaped scaling behavior for MD simulations of uniaxial compression that use a zero-temperature heat bath in the  $b \rightarrow 0$  limit.

TABLE III. Parameters for the linear transformations of  $\sigma_{\max}$  and  $\log_{10} \dot{\epsilon}_{\text{eng}}$  in Eq. (8) that map the experimental data in Fig. 1 to one of four representative MD simulations of  $\text{Ni}_{62}\text{Nb}_{38}$  (EAM) undergoing uniaxial compression: (1)  $T_0 = 0$  K,  $b = 10^{-5}$  eV ps  $\text{\AA}^{-2}$ ; (2)  $T_0 = 0$  K,  $b = 10^{-3}$  eV ps  $\text{\AA}^{-2}$ ; (3)  $T_0 = 40$  K,  $b = 6 \times 10^{-5}$  eV ps  $\text{\AA}^{-2}$ ; and (4)  $T_0 = 40$  K,  $b = 5 \times 10^{-4}$  eV ps  $\text{\AA}^{-2}$  (see Fig. 8). Here,  $c_{\dot{\epsilon},e} = -\eta_{\dot{\epsilon},e} \log_{10} k_{\dot{\epsilon},e}$ .

Metallic glasses	$k_{\sigma,e}$	$c_{\sigma,e}$	$\eta_{\dot{\epsilon},e}$	$c_{\dot{\epsilon},e}$	$T_0, b$
$\text{Ti}_{40}\text{Zr}_{25}\text{Ni}_8\text{Cu}_9\text{Be}_{18}$	2.49	6.45	0.150	8.30	(3)
$\text{Ti}_{45}\text{Zr}_{16}\text{Ni}_9\text{Cu}_{10}\text{Be}_{20}$	13.1	-14.5	0.233	9.93	(2)
$\text{Zr}_{53}\text{Cu}_{30}\text{Ni}_9\text{Al}_8$	3.12	5.81	0.356	8.11	(4)
$\text{Ni}_{62}\text{Nb}_{38}$	1.36	7.49	0.228	9.68	(2)
$\text{Zr}_{50.7}\text{Cu}_{28}\text{Ni}_9\text{Al}_{12.3}$	1.26	8.86	0.370	7.26	(1)
$\text{Zr}_{52.5}\text{Cu}_{17.9}\text{Ni}_{14.6}\text{Al}_{10}\text{Ti}_5$	0.962	9.53	0.490	6.98	(1)
$\text{Zr}_{64.13}\text{Cu}_{15.75}\text{Ni}_{10.12}\text{Al}_{10}$	0.714	10.1	1.50	1.95	(1)
$\text{Zr}_{41.2}\text{Ti}_{13.8}\text{Cu}_{12.5}\text{Ni}_{10}\text{Be}_{22.5}$	3.78	3.97	0.157	8.93	(2)
$\text{Zr}_{59.3}\text{Cu}_{28.8}\text{Nb}_{1.5}\text{Al}_{10.4}$	1.80	8.04	0.541	7.98	(1)
$\text{Pd}_{40}\text{Ni}_{40}\text{P}_{20}$	3.92	4.55	0.389	7.74	(1)
$\text{Ti}_{32.8}\text{Zr}_{30.2}\text{Cu}_9\text{Ni}_{5.3}\text{Be}_{22.7}$	1.15	8.97	0.408	7.65	(1)
$\text{Zr}_{38}\text{Ti}_{17}\text{Cu}_{10.5}\text{Co}_{12}\text{Be}_{22.5}$	1.42	8.54	0.435	7.92	(1)

power law with decreasing  $T^\dagger$  in the high-strain-rate branch. Hence the MD simulation results for  $\text{Ni}_{62}\text{Nb}_{38}$  (modeled with an EAM atomic interaction) can also be mapped to the compressive-strength-versus-temperature curve from MD simulations of  $\text{Zr}_{60}\text{Cu}_{29}\text{Al}_{11}$  (modeled using an EAM atomic interaction) and  $\text{Ni}_{62}\text{Nb}_{38}$  (modeled using the LJ atomic interaction).

We now compare the experimental data for the compressive strength of metallic glasses [5,9–19] in Fig. 1 with the results for the compressive strength from the MD simulations of  $\text{Ni}_{62}\text{Nb}_{38}$  (modeled using EAM atomic interactions) undergoing uniaxial compression. Since the experiments do not provide measurements of the local temperature of the sample, we first identify the best match for each of the 12 experimental data sets for  $\sigma_{\max}$  versus  $\dot{\epsilon}_{\text{eng}}$  with the data from one of four representative MD simulations of  $\text{Ni}_{62}\text{Nb}_{38}$  after applying linear transformations in  $\sigma_{\max}$  and  $\log_{10} \dot{\epsilon}$ :

$$\begin{aligned} \sigma_{\max}^\dagger &= k_{\sigma,e} \sigma_{\max} + c_{\sigma,e}, \\ \dot{\epsilon}_{\text{eng}}^\dagger &= \left( \frac{\dot{\epsilon}_{\text{eng}}}{k_{\dot{\epsilon},e}} \right)^{\eta_{\dot{\epsilon},e}}, \end{aligned} \quad (8)$$

where the scaling parameters  $k_{\sigma,e}$ ,  $c_{\sigma,e}$ ,  $k_{\dot{\epsilon},e}$ , and  $\eta_{\dot{\epsilon},e}$  are provided in Table III of Appendix E. The four representative MD simulations have different combinations of  $T_0$  and  $b$ : (1)  $T_0 = 0$  K,  $b = 10^{-5}$  eV ps  $\text{\AA}^{-2}$ ; (2)  $T_0 = 0$  K,  $b = 10^{-3}$  eV ps  $\text{\AA}^{-2}$ ; (3)  $T_0 = 40$  K,  $b = 6 \times 10^{-5}$  eV ps  $\text{\AA}^{-2}$ ; and (4)  $T_0 = 40$  K,  $b = 5 \times 10^{-4}$  eV ps  $\text{\AA}^{-2}$ . This set of linear transformations is denoted as method II.

We then use the scaled temperature  $T^\dagger$  versus strain rate  $\dot{\epsilon}_{\text{eng}}^\dagger$  from the appropriate representative MD simulation [cf. Eq. (6)] to infer the compressive strength  $\sigma_{\max}^\dagger$  versus temperature  $T^\dagger$  for each of the experimental data sets. In Fig. 8, we show that the  $\sigma_{\max}^\dagger$ -versus- $T^\dagger$  curves for the experimental data are similar to the data for the MD simulations in Fig. 7. In Appendix E, we validate the scaling approach by comparing the results obtained from methods I and II using only

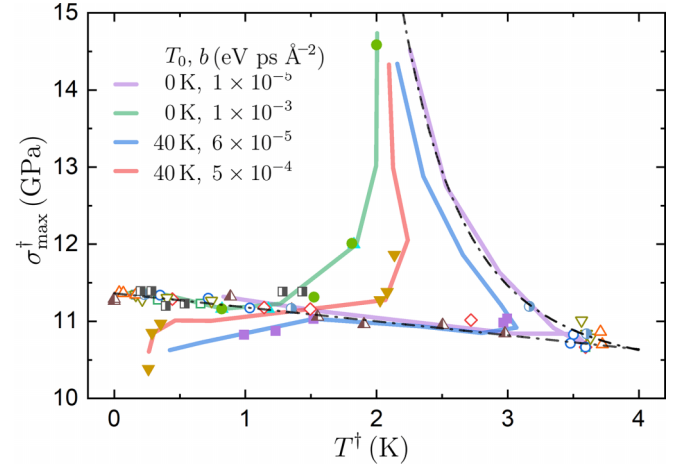


FIG. 8. Scaled compressive strength  $\sigma_{\max}^\dagger$  vs scaled temperature  $T^\dagger$  from experimental studies of uniaxial compression of metallic glasses (using the same symbols as in Fig. 1) collapsed onto one of four representative simulation studies of  $\text{Ni}_{62}\text{Nb}_{38}$  (modeled using EAM atomic interactions) undergoing uniaxial compression with different combinations of the heat bath temperature and damping coefficient ( $T_0 = 0$  K,  $b = 10^{-5}$  eV ps  $\text{\AA}^{-2}$ ;  $T_0 = 0$  K,  $b = 10^{-3}$  eV ps  $\text{\AA}^{-2}$ ;  $T_0 = 40$  K,  $b = 6 \times 10^{-5}$  eV ps  $\text{\AA}^{-2}$ ; and  $T_0 = 40$  K,  $b = 5 \times 10^{-4}$  eV ps  $\text{\AA}^{-2}$ ) indicated by the solid lines. The dash-dotted lines indicate the chevron-shaped scaling behavior for simulations with a zero-temperature heat bath in the  $b \rightarrow 0$  limit.

the MD simulation data on  $\text{Ni}_{62}\text{Nb}_{38}$  (modeled with EAM atomic interactions) for  $\sigma_{\max}^*(T^*)$  and  $\sigma_{\max}^*(\dot{\epsilon}_{\text{eng}})$ , separately. The qualitative agreement of the compressive strength versus temperature for both the simulation and experimental results suggests that the mechanical response of metallic glasses under uniaxial compression can be described by the general deformation mechanisms included in the MD simulations.

#### D. Deformation mechanisms

In Fig. 9, we provide a sketch of the chevron-shaped scaling curve for the compressive strength  $\sigma_{\max}^\dagger$  versus temperature  $T^\dagger$  for metallic glasses undergoing uniaxial compression, which illustrates its main features. In driven, thermal systems, such as metallic glasses undergoing uniaxial compression, thermal fluctuations can arise from the heat bath to which the system is coupled or from the applied deformation. When the influence of the heat bath is small, i.e., for simulated systems coupled to a low-temperature heat bath, the compressive strength versus temperature can be described as a chevron-shaped curve with two main branches—the linear lower branch and power-law upper branch—as shown in Fig. 9. In the lower branch, the mechanical response is primarily driven by localized shear transformation zones (STZs). The STZs cause serrations in the stress-versus-strain curve, where quasilinear increases in stress are punctuated by rapid stress drops, as shown in Fig. 2(a). Higher strain rates in the lower branch of the chevron-shaped curve give rise to local effective heating of the system since there is less time per strain to dissipate the increased kinetic energy generated by the increased strain rate. Thus thermal softening (i.e., negative strain rate sensitivity of the compressive strength)



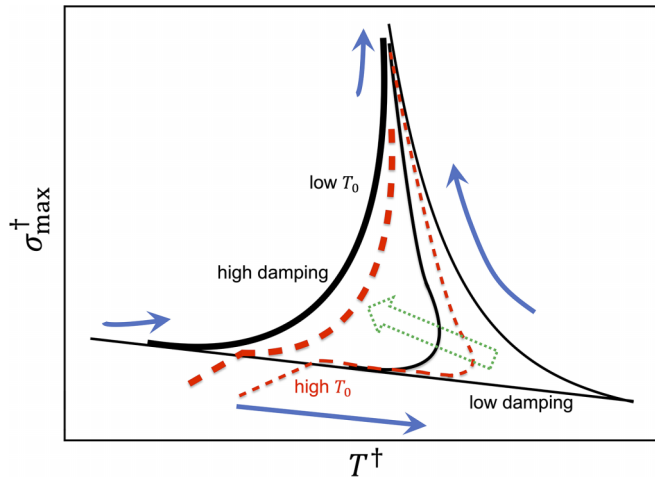


FIG. 9. Sketch of the scaled compressive strength  $\sigma_{\max}^{\dagger}$  plotted as a function of the scaled temperature  $T^{\dagger}$  for metallic glasses undergoing uniaxial compression and coupled to low-temperature (black solid lines) and high-temperature (red dashed lines) heat baths. The hollow arrow signifies the direction of increasing damping coefficient, while the thin solid blue arrows indicate the direction of increasing strain rate.

occurs in the lower branch. In contrast, the power-law upper branch at high strain rates corresponds to more homogeneous deformation and nonserrated stress-versus-strain curves. The more rapid compression process leads to increased potential energy, which cannot be converted rapidly into kinetic energy in the high-strain-rate regime. Therefore the thermal activation of shear transformation zones decreases in this regime, which leads to an increase in the compressive strength (i.e., positive strain rate sensitivity of the compressive strength).

For systems coupled to higher-temperature heat baths, we find a transition of the strain rate sensitivity of the compressive strength from positive to negative at low to intermediate strain rates, in addition to a transition from negative to positive strain rate sensitivity of the compressive strength from intermediate to high strain rates, as shown in Fig. 9. The positive strain rate sensitivity of the compressive strength in the low-strain-rate regime arises from thermally activated barrier hopping in the potential energy landscape since low strain rates allow the system to identify pathways to escape from the current potential energy basin [27]. In contrast to the power-law upper branch with positive strain rate sensitivity of  $\sigma_{\max}^{\dagger}$  at high strain rates, the temperature increases with strain rate in the low-strain-rate regime with positive strain rate sensitivity.

#### IV. CONCLUSIONS AND FUTURE DIRECTIONS

Using MD simulations of metallic glasses ( $\text{Ni}_{62}\text{Nb}_{38}$  and  $\text{Zr}_{60}\text{Cu}_{29}\text{Al}_{11}$ ) undergoing uniaxial compression, we investigate the role of thermal fluctuations in determining the strain rate sensitivity of the compressive strength. When we consider metallic glass samples coupled to a zero-temperature heat bath, we show that the compressive strength versus temperature obeys a chevron-shaped scaling curve in the small-damping-parameter limit. The scaling curve possesses

two branches: The linear lower branch with negative strain rate sensitivity and the power-law upper branch with positive strain rate sensitivity. For systems with nonzero-temperature heat baths, the compressive strength versus temperature deviates from the scaling curve at low strain rates, where the compressive strength initially increases with temperature, but it rejoins the scaling curve as the strain rate increases. Higher values of the damping coefficient also cause the compressive strength to deviate from the chevron-shaped scaling curve at low strain rates, but the compressive strength converges to the scaling curve at high strain rates. For all bath temperatures, we find a range of damping coefficients over which the compressive strength is nonmonotonic in strain rate. We also compare the results from the MD simulations of  $\text{Ni}_{62}\text{Nb}_{38}$  and  $\text{Zr}_{60}\text{Cu}_{29}\text{Al}_{11}$  with experimental results for the compressive strength of 12 metallic glasses [5,9–19]. Each of the alloys obeys a different unscaled-compressive-strength-versus-strain-rate relation. However, we show that the compressive-strength-versus-strain-rate data from these diverse alloys can be mapped (using linear transformations) onto the same chevron-shaped  $\sigma_{\max}^{\dagger}$ -versus- $T^{\dagger}$  scaling curves as found in the MD simulations of  $\text{Ni}_{62}\text{Nb}_{38}$  and  $\text{Zr}_{60}\text{Cu}_{29}\text{Al}_{11}$ . These results suggest that the chevron-shaped scaling behavior, which is determined by local temperature fluctuations and internal dissipation, controls the mechanical response of metallic glasses at finite strain rates and provides a general framework for understanding the strain rate sensitivity of the compressive strength of metallic glasses.

In this paper, we focused on the uniaxial compression of metallic glasses at finite strain rates. However, we also believe that our results will hold for other deformations, such as pure shear and bending, applied to metallic glasses at finite rates. Furthermore, our work emphasizes that internal heating and dissipation mechanisms control the strain-rate-dependent mechanical response. Thus, in future computational studies, we can calculate the local damping coefficients that correspond to nonaffine collective motions of atoms, or shear transformation zones, that give rise to local heating and dissipation. For example, in recent work [25] we developed an exact method to identify and track local deformations during stress drops that result from athermal, quasistatic simple shear applied to model glasses. In future studies, we will generalize the methods for identifying shear transformation zones [28–31] in metallic glasses deformed at finite strain rate and temperature. In addition, this paper focused on the preyield regime without shear bands [32–35]. Predicting the formation and propagation of large-scale shear bands as the system transitions from the preyield regime to the postyield regime is an active area of our future research.

#### ACKNOWLEDGMENTS

We acknowledge support from NSF Grants No. CMMI-1901959 (W.J., A.D., U.D.S., and C.S.O.) and No. CBET-2002797 (M.D.S.). This work was also supported by the high-performance computing facilities operated by Yale's Center for Research Computing.

## APPENDIX A: INTERATOMIC POTENTIALS

We consider both embedded atom method (EAM) and Lennard-Jones interatomic potentials to model  $\text{Ni}_{62}\text{Nb}_{38}$  and  $\text{Zr}_{60}\text{Cu}_{29}\text{Al}_{11}$  metallic glasses undergoing uniaxial compression.

### 1. Embedded atom method

For EAM interaction potentials, the total potential energy is  $U = \sum_i U_i$ , where the potential energy  $U_i$  for each atom  $i$  includes both many-body and pairwise contributions:

$$U_i = f_\alpha \left( \sum_{j \neq i} \rho_\beta(r_{ij}) \right) + \frac{1}{2} \sum_{j \neq i} \varphi_{\alpha\beta}(r_{ij}), \quad (\text{A1})$$

where  $r_{ij}$  is the center-to-center separation between atoms  $i$  and  $j$ , the many-body embedding function  $f_\alpha$  depends on the electron density  $\rho_\beta$ ,  $\varphi_{\alpha\beta}$  is the pairwise potential energy function, and  $\alpha, \beta = \text{A, B}$  are labels for the element types [36]. The summation is over all neighbors  $j$  of atom  $i$  within a cutoff distance  $r_c = 6.9$  and  $6.5 \text{ \AA}$  for  $\text{Ni}_{62}\text{Nb}_{38}$  [21] and  $\text{Zr}_{60}\text{Cu}_{29}\text{Al}_{11}$  [22], respectively. Note that the forms of the embedding function and pairwise potential are specific to each alloy.

### 2. Lennard-Jones pairwise interactions

We also employ a pairwise Lennard-Jones interaction potential to model  $\text{Ni}_{62}\text{Nb}_{38}$  metallic glasses. We assume that atom types  $\alpha, \beta = \text{A, B}$ , which represent Nb and Ni, interact via the truncated and force-shifted Lennard-Jones (LJ) potential:

$$U_{\alpha\beta}(r_{ij}) = \phi_{\alpha\beta}(r_{ij}) - \phi_{\alpha\beta}(r_c) - (r_{ij} - r_c) \left. \frac{d\phi_{\alpha\beta}}{dr_{ij}} \right|_{r_{ij}=r_c}, \quad (\text{A2})$$

where  $r_{ij}$  is the center-to-center separation between atoms  $i$  and  $j$ , the cutoff distance  $r_c = 2.5\sigma_{\alpha\beta}$ , and

$$\phi_{\alpha\beta}(r_{ij}) = 4\epsilon_{\alpha\beta} \left[ \left( \frac{\sigma_{\alpha\beta}}{r_{ij}} \right)^{12} - \left( \frac{\sigma_{\alpha\beta}}{r_{ij}} \right)^6 \right]. \quad (\text{A3})$$

The total potential energy is  $U = \sum_{i>j} U_{\alpha\beta}(r_{ij})$ . The parameters  $\sigma_{\text{BB}}/\sigma_{\text{AA}} = 0.84$ ,  $\sigma_{\text{AB}} = (\sigma_{\text{AA}} + \sigma_{\text{BB}})/2$ , and  $\epsilon_{\text{BB}}/\epsilon_{\text{AA}} = 0.5863$  were chosen to match the relative sizes and cohesive energies of Nb and Ni. The heat of mixing  $\Delta H_{\text{mix}}$  from experiments is used to set  $\epsilon_{\text{AB}}/\epsilon_{\text{AA}} = (1 + \epsilon_{\text{BB}}/\epsilon_{\text{AA}})/2 - \Delta H_{\text{mix}}/\epsilon_{\text{AA}} = 0.83425$  [37]. The mass ratio for NiNb alloys is  $m_{\text{A}}/m_{\text{B}} = 1.583$ .

To compare the MD simulation results for uniaxial compression of  $\text{Ni}_{62}\text{Nb}_{38}$  using the LJ potential with those for the EAM potential [21], we set  $\sigma_{\text{AA}} = 3.0 \text{ \AA}$  for the atomic diameter and  $m_{\text{A}} = 92.91 \text{ amu}$  for the mass of Nb. To determine the cohesive energy scale  $\epsilon_{\text{AA}}/k_{\text{B}}$ , we calculate the position fluctuations of atoms in  $\text{Ni}_{62}\text{Nb}_{38}$  glasses as a function of temperature. We measure the mean-square displacement (MSD),

$$\text{MSD}(t) = \left\langle \frac{1}{N} \sum_{i=1}^N (\mathbf{r}_i(t) - \mathbf{r}_i(0))^2 \right\rangle, \quad (\text{A4})$$

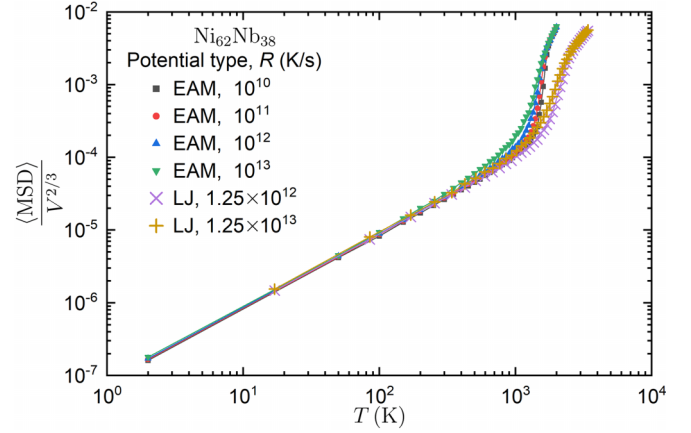


FIG. 10. Mean-square displacement at short times,  $\langle \text{MSD}(t_s) \rangle / V^{2/3}$ , normalized by the surface area of the sample,  $V^{2/3}$ , plotted as a function of temperature  $T$  for EAM and LJ simulations of  $\text{Ni}_{62}\text{Nb}_{38}$ . The temperatures of the LJ systems were scaled by  $\epsilon_{\text{AA}}/k_{\text{B}} = 3400 \text{ K}$  so that they collapse onto the data for the EAM simulations at low temperatures. Data are shown for four EAM and two LJ simulations with samples prepared at different cooling rates  $R$ .

where  $\mathbf{r}_i(t)$  is the position of atom  $i$  at time  $t$  and the angle brackets indicate an average over time origins. In Fig. 10, we show the mean-square displacement at short times ( $t_s = 20 \text{ ps}$  in the EAM simulations and  $t_s = 20\epsilon_{\text{AA}}/k_{\text{B}} \approx 10.9 \text{ ps}$  in the LJ simulations) as a function of temperature for EAM and LJ models of  $\text{Ni}_{62}\text{Nb}_{38}$  that were first rapidly cooled to low temperature and then successively heated above the glass transition temperature. We find that by choosing  $\epsilon_{\text{AA}}/k_{\text{B}} = 3400 \text{ K}$  we can scale the  $\text{MSD}(t_s)$  for the LJ simulations onto those for the EAM simulations for temperatures below the glass transition temperature.

## APPENDIX B: EAM SIMULATIONS OF $\text{Ni}_{62}\text{Nb}_{38}$ IN FINITE-TEMPERATURE HEAT BATHS

In this Appendix, we show the cooling-rate-scaled compressive strength  $\sigma_{\text{max}}^*$  as a function of  $\dot{\epsilon}_{\text{eng}}$  obtained from

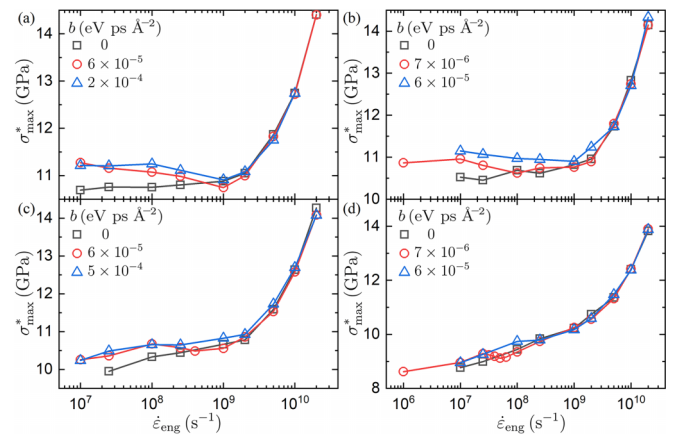


FIG. 11. Cooling-rate-scaled compressive strength  $\sigma_{\text{max}}^*$  plotted vs strain rate  $\dot{\epsilon}_{\text{eng}}$  for  $\text{Ni}_{62}\text{Nb}_{38}$  (EAM) coupled to heat baths with (a)  $T_0 = 2 \text{ K}$ , (b)  $T_0 = 10 \text{ K}$ , (c)  $T_0 = 40 \text{ K}$ , and (d)  $T_0 = 120 \text{ K}$ , with different damping coefficients  $b$ .

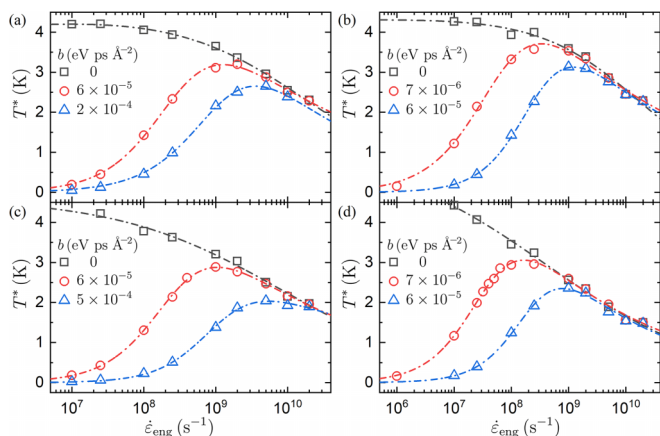


FIG. 12. Cooling-rate-scaled temperature  $T^*$  plotted vs strain rate  $\dot{\epsilon}_{\text{eng}}$  for  $\text{Ni}_{62}\text{Nb}_{38}$  (EAM) coupled to heat baths with (a)  $T_0 = 2$  K, (b)  $T_0 = 10$  K, (c)  $T_0 = 40$  K, and (d)  $T_0 = 120$  K, with different damping coefficients  $b$ . Best fits of  $T^*(\dot{\epsilon}_{\text{eng}})$  to Eq. (6) for different  $b$  values are shown as dash-dotted lines.

MD simulations of  $\text{Ni}_{62}\text{Nb}_{38}$  metallic glasses (using an EAM interatomic potential) undergoing uniaxial compression and coupled to heat baths over a range of temperatures:  $T_0 = 2, 10, 40,$  and  $120$  K. In Fig. 11, we find that the strain rate regime, over which the compressive strength decreases with strain rate, narrows with increasing heat bath temperature and is observed at lower damping coefficients. Unlike systems coupled to low-temperature heat baths, where  $\sigma_{\text{max}}^*$  generally decreases linearly with  $\dot{\epsilon}_{\text{eng}}$  in the low-strain-rate regime,  $\sigma_{\text{max}}^*$  initially increases with  $\dot{\epsilon}_{\text{eng}}$  for systems coupled to high-temperature heat baths. For systems with nonzero-temperature heat baths, the temperature during compression also follows the  $T^*$ -versus- $\dot{\epsilon}_{\text{eng}}$  relation in Eq. (6), as shown in Fig. 12. The fitting parameters to Eq. (6) are provided

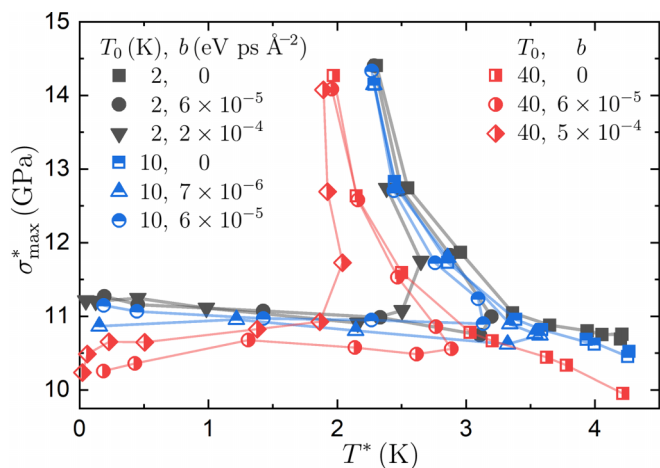


FIG. 13. Cooling-rate-scaled compressive strength  $\sigma_{\text{max}}^*$  plotted vs cooling-rate-scaled temperature  $T^*$  from MD simulations of  $\text{Ni}_{62}\text{Nb}_{38}$  (EAM) undergoing uniaxial compression and coupled to nonzero-temperature heat baths. These data correspond to the same data in Figs. 11(a)–11(c) and 12(a)–12(c). The MD simulations with different damping coefficients are represented by distinct symbols, and the data for  $T_0 = 2, 10,$  and  $40$  K are differentiated by the use of fully filled, top-filled, and right-filled symbols, respectively.

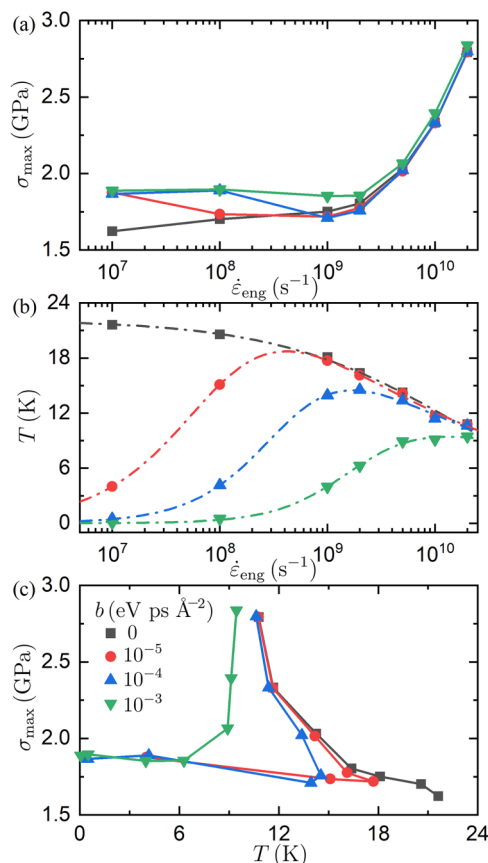


FIG. 14. (a) Compressive strength  $\sigma_{\text{max}}$  plotted as a function of strain rate  $\dot{\epsilon}_{\text{eng}}$  for  $\text{Zr}_{60}\text{Cu}_{29}\text{Al}_{11}$  (modeled using EAM atomic interactions) undergoing uniaxial compression and coupled to a zero-temperature heat bath. The metallic glass samples were prepared using cooling rate  $R = 10^{12}$  K/s. Each data point represents an average of 20 independently generated samples, and different symbols indicate varying  $b$  values. (b) Average temperature  $T$  (over the strain interval  $0 < \epsilon_{\text{eng}} < 0.076$ ) for the data in (a) plotted vs strain rate  $\dot{\epsilon}_{\text{eng}}$ . Best fits of  $T(\dot{\epsilon}_{\text{eng}})$  to Eq. (6) for different  $b$  values are shown as dash-dotted lines. (c) Compressive strength  $\sigma_{\text{max}}$  plotted vs average temperature  $T$  for data in (a) and (b).

in Table I of Appendix E. As discussed in Sec. III B, for systems with nonzero-temperature heat baths,  $\sigma_{\text{max}}^*$  versus  $T^*$  deviates from the scaling curve at low strain rates but rejoins the scaling curve at large strain rates, as shown in Fig. 13.

### APPENDIX C: EAM SIMULATIONS OF $\text{Zr}_{60}\text{Cu}_{29}\text{Al}_{11}$ IN ZERO-TEMPERATURE HEAT BATHS

In this Appendix, we provide additional details concerning the MD simulations of uniaxial compression of  $\text{Zr}_{60}\text{Cu}_{29}\text{Al}_{11}$  modeled using an EAM potential and coupled to a zero-temperature heat bath. The results for the compressive strength and temperature are similar to those for  $\text{Ni}_{62}\text{Nb}_{38}$  using both the LJ and EAM potentials. In Fig. 14, we show the compressive strength  $\sigma_{\text{max}}$  and strain-averaged temperature  $T$  versus strain rate  $\dot{\epsilon}_{\text{eng}}$  for  $\text{Zr}_{60}\text{Cu}_{29}\text{Al}_{11}$  samples prepared using a cooling rate of  $R = 10^{12}$  K/s. The temperature was obtained by averaging over the strain interval  $0 < \epsilon_{\text{eng}} < 0.076$ , which includes the peak in the compressive

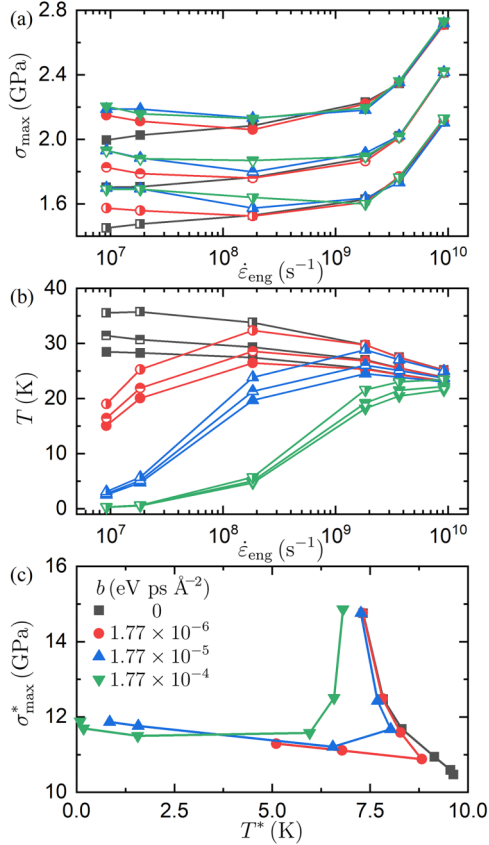


FIG. 15. (a) Compressive strength  $\sigma_{\max}$  vs strain rate  $\dot{\epsilon}_{\text{eng}}$  for LJ simulations of  $\text{Ni}_{62}\text{Nb}_{38}$  undergoing uniaxial compression and coupled to a zero-temperature heat bath. The metallic glass samples were generated at cooling rates  $R = 10^{12}$  (fully filled symbols),  $10^{13}$  (top-filled), and  $10^{14}$  (right-filled) K/s. Each data point represents an average of 45 independently generated samples. (b) Average temperature  $T$  (over the strain interval  $0 < \epsilon_{\text{eng}} < 0.065$ ) for the data in (a) plotted vs strain rate  $\dot{\epsilon}_{\text{eng}}$ . The symbol style is the same as in (a). (c) Cooling-rate-scaled and averaged compressive strength  $\sigma_{\max}^*$  plotted vs the cooling-rate-scaled and averaged temperature  $T^*$  for the data in (a) and (b). In (a)–(c), the different symbols denote the varying damping coefficients.

stress. Again, the compressive strength and average temperature are nonmonotonic as a function of strain rate for nonzero damping coefficients, as shown in Fig. 14. We show the relation between the compressive strength  $\sigma_{\max}$  and the average temperature  $T$  for the EAM model of  $\text{Zr}_{60}\text{Cu}_{29}\text{Al}_{11}$  in Fig. 14(c). We find qualitatively similar behavior for  $\sigma_{\max}$  versus  $T$  for EAM simulations of both  $\text{Zr}_{60}\text{Cu}_{29}\text{Al}_{11}$  and  $\text{Ni}_{62}\text{Nb}_{38}$ .

#### APPENDIX D: LENNARD-JONES SIMULATIONS OF $\text{Ni}_{62}\text{Nb}_{38}$ IN ZERO-TEMPERATURE HEAT BATHS

In this Appendix, we describe the results from MD simulations of  $\text{Ni}_{62}\text{Nb}_{38}$  (modeled using Lennard-Jones interactions) undergoing uniaxial compression and coupled to a zero-temperature heat bath. In Figs. 15(a) and 15(b), we plot the compressive strength  $\sigma_{\max}$  and temperature  $T$  as a function of strain rate  $\dot{\epsilon}_{\text{eng}}$ . As found for the EAM simulations of

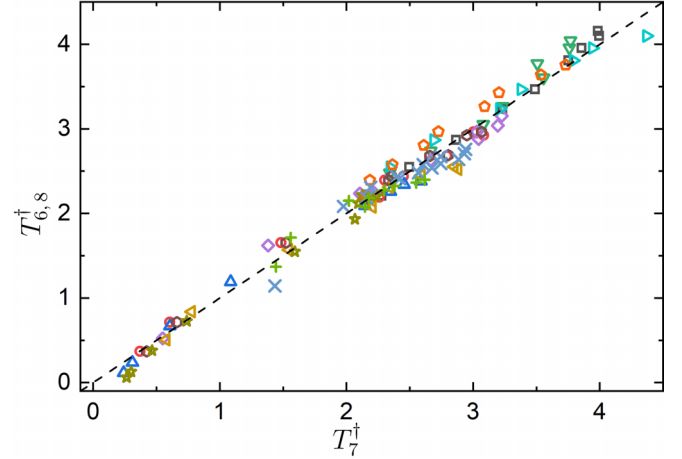


FIG. 16. Comparison of the results for methods I and II for obtaining the scaled temperature,  $T_7^\dagger$  from Eq. (7) and  $T_{6,8}^\dagger$  from Eqs. (6) and (8), using only the MD simulation data of  $\text{Ni}_{62}\text{Nb}_{38}$  (EAM) undergoing uniaxial compression and coupled to nonzero-temperature heat baths. The dashed line indicates  $T_{6,8}^\dagger = T_7^\dagger$ .

$\text{Ni}_{62}\text{Nb}_{38}$ , both  $\sigma_{\max}$  and  $T$  possess nonmonotonic behavior as a function of strain rate. As discussed in Sec. III A, the compressive strength and temperature display self-similar scaling with the cooling rate  $R$ :  $\sigma_{\max}^* = \langle \sigma_{\max}(R/R_c)^\gamma \rangle_R$  and  $T^* = \langle (T - T_0)(R/R_c)^{-\lambda} \rangle_R$ , where  $R_c = 1$  K/s is a reference cooling rate,  $\gamma \approx 0.060$ , and  $\lambda \approx 0.039$  for  $\text{Ni}_{62}\text{Nb}_{38}$  with LJ interactions. In Fig. 15(c), we show the relation between the cooling-rate-scaled compressive strength  $\sigma_{\max}^*$  and the cooling-rate-scaled temperature  $T^*$  for the LJ model of  $\text{Ni}_{62}\text{Nb}_{38}$ .  $\sigma_{\max}^*$  versus  $T^*$  for the LJ simulations is similar to that for the EAM simulations of  $\text{Ni}_{62}\text{Nb}_{38}$  as shown in Fig. 5. However, the magnitude of the slope of the linear branch for the LJ simulations is half of that from the EAM simulations of  $\text{Ni}_{62}\text{Nb}_{38}$ , and the power-law exponent of the high-strain-rate branch is  $\nu \approx 9.6$ , which is approximately twice the value from the EAM simulations of  $\text{Ni}_{62}\text{Nb}_{38}$ . One possible explanation for the difference in the slopes and power-law exponents of the scaling behavior of  $\sigma_{\max}^*(T^*)$  is the difference in the specific heat obtained for the LJ and EAM potentials of  $\text{Ni}_{62}\text{Nb}_{38}$  [38].

#### APPENDIX E: TABLES OF PARAMETERS IN EQS. (6)–(8) AND COMPARISON OF TEMPERATURE SCALING METHODS

As described in Sec. III C, the mapping of  $\sigma_{\max}^*$  versus  $T^*$  for MD simulations that use a nonzero-temperature heat bath onto  $\sigma_{\max}^*$  versus  $T^*$  for MD simulations that use a zero-temperature heat bath involves the linear transformation of  $T^*$  in Eq. (7). We refer to this approach as method I. The mapping of the experimental data of  $\sigma_{\max}$  versus  $\dot{\epsilon}_{\text{eng}}$  onto the scaled MD simulation results for  $\sigma_{\max}^*$  versus  $T^*$  is referred to as method II. For method II, we first linearly scale  $\log_{10} \dot{\epsilon}_{\text{eng}}$  [Eq. (8)] from the experimental data and then determine the corresponding  $T^\dagger$  using Eq. (6) from the MD simulation data. As a test, we can carry out method II on the MD simulation data to obtain  $T_{6,8}^\dagger$  and compare it with  $T_7^\dagger$  from method I

for the same data. In Fig. 16, we show that  $T_{6,8}^{\dagger} \sim T_7^{\dagger}$ , which suggests that methods I and II provide consistent estimates of the temperature.

In this Appendix, we also provide the fitting parameters for quantifying the relationship between temperature and strain rate and parameters of the linear transformations that allow us to compare the results for the compressive strength from different MD simulations and experimental studies of metallic glasses. In Table I, we present the fitting parameters for determining  $T(\dot{\epsilon}_{\text{eng}})$  [Eq. (6)] for Ni<sub>62</sub>Nb<sub>38</sub> (EAM)

systems, both when coupled to zero-temperature heat baths [Fig. 4(b)] and when coupled to nonzero-temperature heat baths (Fig. 12), as well as for Zr<sub>60</sub>Cu<sub>29</sub>Al<sub>11</sub> coupled to zero-temperature heat baths [Fig. 14(b)]. The parameters for Eq. (7) used to map  $\sigma_{\text{max}}^*$  versus  $T^*$  for MD simulations that use a nonzero-temperature heat bath onto  $\sigma_{\text{max}}^*$  versus  $T^*$  for MD simulations using a zero-temperature heat bath are listed in Table II. Finally, the parameters for method II to map the results of the experimental studies onto the results from the MD simulations are provided in Table III.

- 
- [1] J. Schroers and W. L. Johnson, *Phys. Rev. Lett.* **93**, 255506 (2004).
- [2] A. L. Greer and E. Ma, *MRS Bull.* **32**, 611 (2007).
- [3] M. D. Demetriou, M. E. Launey, G. Garrett, J. P. Schramm, D. C. Hofmann, W. L. Johnson, and R. O. Ritchie, *Nat. Mater.* **10**, 123 (2011).
- [4] C. Suryanarayana and A. Inoue, *Bulk Metallic Glasses* (CRC, Boca Raton, FL, 2017).
- [5] J. Lu, G. Ravichandran, and W. L. Johnson, *Acta Mater.* **51**, 3429 (2003).
- [6] A. Dubach, F. H. Dalla Torre, and J. F. Löffler, *Philos. Mag. Lett.* **87**, 695 (2007).
- [7] G. Ma, Z. Zhu, Z. Wang, and H. Zhang, *J. Mater. Sci. Technol.* **31**, 941 (2015).
- [8] J. Lewandowski and A. Greer, *Nat. Mater.* **5**, 15 (2006).
- [9] J. Zhang, J. M. Park, D. H. Kim, and H. S. Kim, *Mater. Sci. Eng.: A* **449-451**, 290 (2007).
- [10] W. Ma, H. Kou, J. Li, H. Chang, and L. Zhou, *J. Alloys Compd.* **472**, 214 (2009).
- [11] T.-H. Chen and C.-K. Tsai, *Materials* **8**, 1831 (2015).
- [12] A. Datye and U. D. Schwarz (unpublished).
- [13] T. Mukai, T. Nieh, Y. Kawamura, A. Inoue, and K. Higashi, *Intermetallics* **10**, 1071 (2002).
- [14] B. P. Wang, L. Wang, Y. F. Xue, S. Y. Wang, Y. Q. Wang, H. F. Zhang, and H. M. Fu, *Mater. Sci. Eng.: A* **609**, 53 (2014).
- [15] Y. F. Xue, H. N. Cai, L. Wang, F. C. Wang, and H. F. Zhang, *Mater. Sci. Eng.: A* **473**, 105 (2008).
- [16] W. Zheng, Y. J. Huang, G. Y. Wang, P. K. Liaw, and J. Shen, *Metall. Mater. Trans. A* **42**, 1491 (2011).
- [17] M. C. Li, M. Q. Jiang, S. Yang, F. Jiang, L. He, and J. Sun, *Mater. Sci. Eng.: A* **680**, 21 (2017).
- [18] W.-D. Liu, K.-X. Liu, X.-X. Xia, and W.-H. Wang, *J. Mater. Res.* **25**, 1230 (2010).
- [19] R. Ramachandramoorthy, F. Yang, D. Casari, M. Stolpe, M. Jain, J. Schwiedrzik, J. Michler, J. J. Kruzic, and J. P. Best, *J. Mater. Res.* **36**, 2325 (2021).
- [20] Y. Yokoyama, T. Yamasaki, P. K. Liaw, and A. Inoue, *Acta Mater.* **56**, 6097 (2008).
- [21] Y. Zhang, R. Ashcraft, M. Mendeleev, C. Wang, and K. Kelton, *J. Chem. Phys.* **145**, 204505 (2016).
- [22] Y. Q. Cheng, E. Ma, and H. W. Sheng, *Phys. Rev. Lett.* **102**, 245501 (2009).
- [23] T. Schneider and E. Stoll, *Phys. Rev. B* **17**, 1302 (1978).
- [24] S. Plimpton, *J. Comput. Phys.* **117**, 1 (1995).
- [25] W. Jin, A. Datye, U. D. Schwarz, M. D. Shattuck, and C. S. O'Hern, *Soft Matter* **17**, 8612 (2021).
- [26] J. Yu, A. Datye, Z. Chen, C. Zhou, O. E. Dagdeviren, J. Schroers, and U. D. Schwarz, *Commun. Mater.* **2**, 22 (2021).
- [27] P. Cao, M. P. Short, and S. Yip, *Proc. Natl. Acad. Sci. USA* **116**, 18790 (2019).
- [28] D. Şopu, A. Stukowski, M. Stoica, and S. Scudino, *Phys. Rev. Lett.* **119**, 195503 (2017).
- [29] H. L. Peng, M. Z. Li, and W. H. Wang, *Phys. Rev. Lett.* **106**, 135503 (2011).
- [30] M. Hassani, A. E. Lagogianni, and F. Varnik, *Phys. Rev. Lett.* **123**, 195502 (2019).
- [31] S. Im, Y. Wang, P. Zhao, G. H. Yoo, Z. Chen, G. Calderon, M. Abbasi Gharacheh, M. Zhu, O. Licata, B. Mazumder, D. A. Muller, E. S. Park, Y. Wang, and J. Hwang, *Phys. Rev. Mater.* **5**, 115604 (2021).
- [32] F. Shimizu, S. Ogata, and J. Li, *Mater. Trans.* **48**, 2923 (2007).
- [33] A. Greer, Y. Cheng, and E. Ma, *Mater. Sci. Eng.: R* **74**, 71 (2013).
- [34] Z. Sha, L. He, S. Xu, Q. Pei, Z. Liu, Y. Zhang, and T. Wang, *Scr. Mater.* **93**, 36 (2014).
- [35] H. Song, S. Li, and Q. Deng, *Comput. Mater. Sci.* **139**, 106 (2017).
- [36] M. S. Daw and M. I. Baskes, *Phys. Rev. Lett.* **50**, 1285 (1983).
- [37] A. Takeuchi and A. Inoue, *Mater. Trans.* **46**, 2817 (2005).
- [38] S. F. Noraldeen, L. Jin, and L. Zhou, *Therm. Sci. Eng. Prog.* **27**, 101157 (2022).